AIAA JOURNAL
Vol. 44, No. 6, June 2006

Elastodynamic Analysis of Aerial Refueling Hose Using Curved Beam Element

Z. H. Zhu* and S. A. Meguid†
University of Toronto, Toronto, Ontario M5S 7G8, Canada

The elastodynamic analysis of an aerial refueling hose by classic cable theory suffers the singularity problem when the hose slackens under dynamic loadings. The difficulty is addressed and overcome by modeling the refueling hose with a new three-noded locking-free curved beam element. The large deformations and rotations of curved beams are formulated in terms of an updated Lagrangian framework with consistently coupled quintic polynomial displacement fields to satisfy the membrane locking-free condition. The stability and accuracy of the new element is validated by experiments involving an instrumented free-swinging steel cable. Good agreement is observed between the experimental results and the predictions of the new element. The numerical capability of modeling a refueling hose and drogue system has been demonstrated by simulating 1) the oscillation of hose due to the disturbance from the tanker and the vortex-induced velocity and 2) a receiver coupling with a hose reel malfunction. The analysis results show clearly the formation and propagation of oscillations along the hose, the consequent whipping near the drogue, and the associated variation of hose tension. The results of new element agree well with field observations and existing analysis results.

I. Introduction

AERIAL refueling hose and drogue systems have been widely used over the years with a growing number of incidents. For instance, it is reported that the hose and drogue system suffered a 2.5% failure rate.[1] Most of the incidents occur when the hose slackens and loses the stabilizing effect of hose tension. The slack may occur during the coupling process of the drogue and probe due to a malfunction of the hose reel mechanism failing to take up the slacking hose, a sudden movement of the tanker, mechanical vibration, wind loading, and/or the poor design of the drogue. As a result, any disturbance to the hose will travel downstream with an increasing magnitude resulting in a whipping action near the drogue. The whipping will generate high tension spikes in the hose that could lead to the separation of drogue from hose. It is, therefore, important to model and analyze accurately the dynamics of the refueling hose and drogue to be able to design robust and efficient systems.

A limited number of studies have been devoted to the analysis of the refueling hose and drogue system.[2–4] The system can be further divided into three subsystems of interest to this work, namely, 1) a reel mechanism in the storage pod on the tanker, 2) a refueling hose, and 3) a drogue. The motion of the pod is generally assumed independent of refueling hose and drogue because the mass and size of the tanker are generally several orders of magnitude larger than the hose and drogue. The refueling hose is usually idealized as a thin cable with a circular section due to its large ratio of length over diameter. Finally, the drogue is generally modeled as a lumped mass (named as towed body). Thus, the aerial refueling hose and drogue system can be idealized as an aerial cable towed system with prescribed motions at the tow point (the tanker).

The dynamic instability of an aerial cable towed system is characterized by large or violent oscillations of the tow cable and the towed body associated with low cable tension. The earliest studies on the subject were carried out during World War I by Bairstow et al.[5] and subsequently by Glauert,[6] among others. The early work by Glauert concentrated on the stability of towed body by ignoring the cable's physical characteristics such as mass, drag, and elasticity. Later works extended the analysis by including rigorous cable dynamics to examine the stability of aerial towed systems more accurately. For instance, DeLaurier[7] assumed the cable to be flexible but inextensible, described by a partial differential equation with the towed body as the boundary condition at its end. Aerodynamic effects such as drag and added mass of the air were included in the analysis. Phillips[8] further studied the effect of perturbation at the tow point on the stability condition of a cable towed system at high speed. His analyses suggested that any small perturbations at the tow point would be amplified along the cable downstream if the airspeed were greater than the wave propagation speed of the cable. Later, the inextensible limitation of the cable was released by DeMatteis,[9] who studied the longitudinal stability of aerial towed systems, including a towing aircraft, an extensible cable, and a towed glider. Nakagawa and Obata[10] conducted further excellent modal analyses of an aerial towed system with a towed body. Their study recognized that 1) the unstable behavior of aerial towed systems around the steady state strongly depends on the cable tension and 2) the aerodynamic characteristics of the towed body and the curvature of tow cable have significant effects on the stability of aerial towed system. In all of these studies, the cable is assumed as a tension member only that cannot resist compressive, bending, and torsional loads. However, unlike high-tension cables where the cable tension is several orders of magnitude higher than the bending and the torsional moments, the basic mechanism of energy propagation in low-tension cables is changed from a membrane dominant state to a bending dominant state.[11] Note that the classic cable theory provides inaccurate results when the cable tension is low and suffers the singularity problem when the cable tension disappears anywhere along the cable.[12] The limitation of its application to low-tension problems is attributed to two reasons. First, it becomes singular if the tension vanishes anywhere in the cable. Second, it neglects the bending stiffness of cable.

The limitations of the existing approaches create a need for alternative approaches to treat low-tension cable problems such as the aerial refueling hoses. Many works[11–15] have been carried out to alleviate the singularity problem associated with the low-tension cables by adding artificial damping, higher-order terms and bending stiffness of the beam. Among them, only the approach based on the beam theory is a natural extension of the classic cable theory and has a sound theoretical foundation and physical meaning.

Received 22 April 2005; revision received 19 October 2005; accepted for publication 31 October 2005.

*Research Associate, Department of Mechanical and Industrial Engineering, 5 King's College Road.

†Professor, Department of Mechanical and Industrial Engineering; currently Head, Aerospace Engineering Division, School of Mechanical and Aerospace Engineering, Nanyang Technological University, 50 Nanyang Avenue, Singapore 639798, Republic of Singapore. Lifetime Member AIAA.

Unfortunately, the modeling of these aerial towed systems with a realistic and robust description of cable dynamics inevitably leads to a complex mathematical problem and consequently requires numerical solution techniques. Many numerical solution techniques have been published in the literature, such as 1) lumped parameter, 2) finite difference, and 3) finite element methods.

The lumped parameter method simplifies the nonlinear partial differential equations of motion into ordinary differential equations by lumping the distributed mass, the external loads, and the inertial force of cable to specified nodes along its length.[13] It is actually a special case of the finite element method.

The finite difference method approximates the governing equations of the cable by some difference equations along its length.[11,14,15] Solutions of cable dynamics using the finite difference method are very popular and attractive because of their simplicity. However, the finite difference method is problem specific and cannot be implemented in general-purpose analysis programs for complex geometries with multiple cable branches or different cable properties along the cable length.

The finite element method is probably the most appealing technique among all numerical methods. In the finite element method, the cable is discretized into a finite number of elements. The main advantage of the finite element method over the finite difference method is its capability to handle complex geometries with multiple cable branches or different cable properties along the cable length in an algorithmic fashion, allowing for its implementation in general-purpose analysis programs. For applications of high-tension cables, the truss elements are used to discretize the cable.[16] For applications of low-tension cables, the classic cable theory is no longer adequate as we just outlined, and a flexible beam theory must be used to deal with the slack of cable properly. However, the finite element method has not been widely used in modeling the cable dynamics compared with the finite difference method. There are two major difficulties associated with the finite element method in low-tension cable problems compared with the finite difference method. The first is the lack of proper beam element that can properly handle the curvature effect together with large displacements and rotations. The second is that the mathematical formulations of the finite element method of a generalized flexible beam element are more complex than the finite difference method.

There are many types of flexible beam elements available in the literature for modeling cable systems.[17] The simplest one is the two-noded straight element. A detailed review of the straight beam element can be found in the work of Reddy[18] and Chakraborty et al.[19] However, the straight element violates the continuity condition of slope and curvature of a slacking cable by discretizing the curved cable into straight segments. As a result, excessive bending stiffness or membrane locking becomes prevalent.[20] Curved beam elements, which are based on the curvilinear strain field description, have an advantage over their straight counterparts in modeling curved cables by yielding higher accuracy using coarse meshes. However, the formulation of curved beams is not a simple extension of the straight beams because of the so-called locking problem, even for the linear beam theory.[21] Stolarski and Belytschko[22] and Prathap and Bhashyam[23] identified the cause of the locking as the failure of the independently interpolated displacement fields to recover correct constraints from the membrane strain in the state of inextensible bending. Later, Prathap and Bhashyam[24] and Balasubramanian and Prathap[25] proposed a field consistency interpolation method in which the axial displacement field is required to be one order higher than the transverse displacement field. The field consistency concept is the most appealing among the curved beam element formulations because it allows predicting a priori any poor convergence due to locking. To improve the computational efficiency of the field consistency method, lower-order polynomial displacement fields have been developed by coupling the axial and transverse polynomial interpolations through the equilibrium equations to enable the recovery of the inextensible bending mode of a curved beam.[26] Detailed reviews of curved element formulations can be found in the works of Bucalem and Bathe[27] and Raveendranath et al.[26,28,29] Inspired by the concept of coupled consistency displacement fields, Zhu and Meguid[30] proposed a linear three-noded, three-dimensional curved beam element. The inextensible bending mode is recovered by coupling the consistent axial and transverse polynomial interpolations with presumably linear membrane and torsional strain fields, not with the equilibrium equations that will become complicated mathematically in the case of large deformations and rotations. The new element demonstrates higher accuracy, a faster convergence rate, and better computational efficiency. However, the authors are unaware of any work that reports the application of curved beam elements in modeling aerial refueling hose and drogue systems.

In this paper, we address and overcome these difficulties by developing a new nonlinear three-noded curved beam element that is capable of modeling the dynamics of aerial refueling hose based on the earlier proposed linear three-noded curved beam element.[30] The finite element formulation of the new curved beam element is developed by a variational approach using the principle of virtual work in the framework of incremental updated Lagrange description. For the sake of stability and reliability of numerical integration, the predictor–corrector method[31] with a Newmark time-stepping algorithm and a Newton–Raphson iteration is used to solve the equation of motion of the refueling hose. The resulting finite element formulations and the time integration method are implemented in appropriate computer codes and validated by experimental investigations. The new element and codes are then applied to the elastodynamic analysis of a refueling hose and drogue system.

This paper contains five sections. Following this introductory section, in Sec. II, a detailed account of the newly developed curved beam element using updated Lagrangian formulations is provided. In Sec. III, we validate the newly developed curved beam element experimentally using a freely swinging instrumented steel cable. In Sec. IV, we conduct an elastodynamic analysis of an aerial refueling hose using the new element and codes. Finally, in Sec. V, we conclude the paper.

II. Finite Element Formulation of Three-Noded Curved Beam Element

Consider the three-noded curved beam element shown in Fig. 1. A system of convected curvilinear coordinates x_i, $i = 1, 2, 3$, is selected to describe the curved beam and its motion, where x_3 denotes the length along the neutral axis, whereas x_1 and x_2 denote the distances along lines orthogonal to the neutral axis. The incremental translational and rotational displacements of the neutral axis ${}_tu_1$, ${}_tu_2$, ${}_tu_3$, ${}_t\theta_1$, ${}_t\theta_2$, and ${}_t\theta_3$ with respect to the time t configuration are shown in the convected curvilinear coordinate system in their positive directions. The geometry of the curved element will be described by its length ${}^tL$ and curvature ${}^t\kappa$, whereas the position and the orientation of the element in space will be determined by its nodal coordinates X_i, $i = 1, 2, 3$, in a global Cartesian coordinate system. The transformation between the global and local coordinates will be established in accordance with Ref. 32.

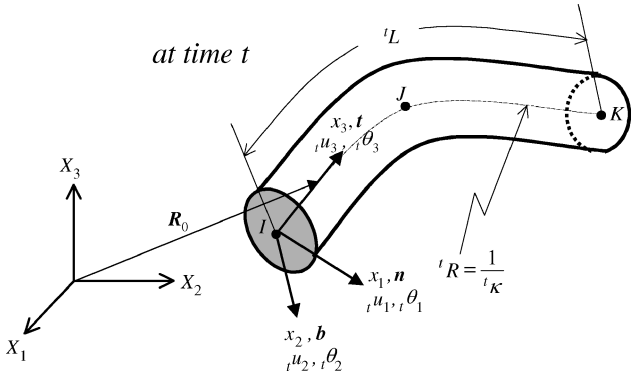

Fig. 1 Three-dimensional curved beam element in curvilinear coordinates.

The incremental Green–Lagrange strains of the curved beam at time $t+\Delta t$ are defined with respect to time t (Ref. 33):

$$ {}_tE_{33} = {}_t\varepsilon - x_1\left({}_t\omega_2 - 2{}^t\kappa_t\varepsilon\right) + x_2{}_t\omega_1 $$
$$ {}_tE_{13} = -(x_2/2)_t\eta, \qquad {}_tE_{23} = (x_1/2)_t\eta \tag{1} $$

where ${}_t\varepsilon$, ${}_t\omega_1$, ${}_t\omega_2$, and ${}_t\eta$ are the incremental membrane strain and curvature rates of the neutral axis and can be expressed in terms of the displacements of the neutral axis,

$$ {}_t\varepsilon = {}_tu_{3,3} - {}^t\kappa_t u_1 + \underline{\tfrac{1}{2}\left[\left({}_tu_{1,3} + {}^t\kappa_t u_1\right)^2 + ({}_tu_{2,3})^2 + \left({}_tu_{3,3} - {}^t\kappa_t u_1\right)^2\right]} \tag{2a} $$

$$ {}_t\omega_1 = -{}_tu_{2,33} + {}^t\kappa_t\theta_3 + \underline{{}_t\theta_3\left({}_tu_{1,33} + 2{}^t\kappa_t u_{3,3} - {}^t\kappa^2{}_tu_1\right)} $$
$$ \underline{+{}_tu_{2,3}\left({}_tu_{3,33} - 2{}^t\kappa_t u_{1,3} - {}^t\kappa^2{}_tu_3\right)} \tag{2b} $$

$$ {}_t\omega_2 = {}_tu_{1,33} + {}^t\kappa_t u_{3,3} + {}^t\kappa_t\varepsilon^L + \underline{{}_t\theta_3{}_tu_{2,33} - \left({}_tu_{1,3} + {}^t\kappa_t u_3\right)\left({}_tu_{3,33} - 2{}^t\kappa_t u_{1,3} - {}^t\kappa^2{}_tu_3\right)} \tag{2c} $$

$$ {}_t\eta = {}_t\theta_{3,3} + {}^t\kappa_t u_{2,3} + \underline{{}^t\kappa_t\theta_3\left({}_tu_{1,3} + {}^t\kappa_t u_3\right) + {}_tu_{2,3}\left({}_tu_{1,33} + {}^t\kappa_t u_{3,3}\right)} \tag{2d} $$

The underlined terms in these expressions are the nonlinear parts of the incremental membrane strain and curvature rates of the neutral axis due to large displacements and rotations.

From Hooke's law, we derive the incremental constitutive relationships of the curved beam as

$$ {}_tT = {}_tE{}^tA_t\varepsilon + \underline{{}_tu_{3,3}{}^{t+\Delta t}T + {}_t\theta_{1,3}{}^{t+\Delta t}M_1 + {}_t\theta_{2,3}{}^{t+\Delta t}M_2} \tag{3a} $$

$$ {}_tM_1 = {}_tE{}^tI_{1t}\omega_1 + \underline{{}_tu_{3,3}{}^{t+\Delta t}M_1 + {}^{t+\Delta t}M_3{}_t\theta_2{}^tI_1/{}^tJ + {}^{t+\Delta t}T_t\theta_{1,3}{}^tI_1/{}^tA} \tag{3b} $$

$$ {}_tM_2 = {}_tE{}^tI_{2t}\omega_2 + \underline{{}_tu_{3,3}{}^{t+\Delta t}M_2 - {}^{t+\Delta t}M_3{}_t\theta_1{}^tI_2/{}^tJ + {}^{t+\Delta t}T_t\theta_{2,3}{}^tI_2/{}^tA} \tag{3c} $$

$$ {}_tM_3 = {}_tG{}^tJ_t\eta + \underline{-{}_tu_{1,3}{}^{t+\Delta t}M_1 - {}_tu_{2,3}{}^{t+\Delta t}M_2 + {}^{t+\Delta t}T_t\theta_{3,3}{}^tJ/{}^tA} \tag{3d} $$

where ${}_tT$ and ${}_tM_i$, $i=1,2,3$, are the incremental tension, bending, and torsional moments; ${}_tE$ and ${}_tG$ are Young's and shear moduli; ${}^tA$, ${}^tI_i$, $i=1,2$, and ${}^tJ$ are the area, principal, and polar inertia moments of the cross section of the beam; and the underlined terms are the nonlinear increments due to the large displacements and rotations, respectively.

Assume that the displacement interpolations for the three-noded curved beam element can be written as

$$ {}_tu_1 = a_0 + a_1x_3 + a_2x_3^2 + a_3x_3^3 + a_4x_3^4 + a_5x_3^5 \tag{4a} $$

$$ {}_tu_2 = b_0 + b_1x_3 + b_2x_3^2 + b_3x_3^3 + b_4x_3^4 + b_5x_3^5 \tag{4b} $$

$$ {}_tu_3 = a_6 + a_7x_3 + a_8x_3^2 + ({}^t\kappa/3)a_2x_3^3 + ({}^t\kappa/4)a_3x_3^4 + ({}^t\kappa/5)a_4x_3^5 + ({}^t\kappa/6)a_5x_3^6 \tag{4c} $$

$$ {}_t\theta_1 = -b_1 - 2b_2x_3 - 3b_3x_3^2 - 4b_4x_3^3 - 5b_5x_3^4 \tag{4d} $$

$$ {}_t\theta_2 = \left(a_1 + {}^t\kappa a_6\right) + \left(2a_2 + {}^t\kappa a_7\right)x_3 + \left(3a_3 + {}^t\kappa a_8\right)x_3^2 + \left[4a_4 + ({}^t\kappa^2/3)a_2\right]x_3^3 + \left[5a_5 + ({}^t\kappa^2/4)a_3\right]x_3^4 + ({}^t\kappa^2/5)a_4x_3^5 + ({}^t\kappa^2/6)a_5x_3^6 \tag{4e} $$

$$ {}_t\theta_3 = b_6 + b_7x_3 + b_8x_3^2 - {}^t\kappa b_3x_3^3 - {}^t\kappa b_4x_3^4 - {}^t\kappa b_5x_3^5 \tag{4f} $$

where a_i and b_i are the coefficients of the interpolation functions and ${}^t\kappa$ is the curvature of the curved beam element, respectively.

When the displacements ${}_tu_1$ and ${}_tu_3$ are substituted into Eq. (2a) and the higher-order terms are ignored, the inextensible bending condition can be written as

$$ {}_t\varepsilon = a_7 - {}^t\kappa a_0 + \left(2a_8 - {}^t\kappa a_1\right)x_3 = 0 $$

or

$$ a_7 - {}^t\kappa a_0 = 0, \qquad 2a_8 - {}^t\kappa a_1 = 0 \tag{5} $$

Equation (5) shows that there are no spurious terms in the constraint equations because each constraint equation contains the contributions from the axial and transverse displacement fields. Thus, the proposed displacement fields are able to recover the inextensible bending mode of the curved beam element, which ensures that the proposed interpolations are free from the membrane locking.

The incremental principle of virtual work at time $t+\Delta t$ with respect to the reference configuration at time t in the updated Lagrangian description can be written as

$$ \int_{{}_tL}\left({}^{t+\Delta t}T\delta{}_t\varepsilon + \sum_{i=1}^{2}{}^{t+\Delta t}M_i\delta{}_t\omega_i + {}^{t+\Delta t}M_3\delta{}_t\eta\right)\mathrm{d}x_3 + \int_{{}_tL}{}^{t+\Delta t}\rho\left({}^{t+\Delta t}A\sum_{i=1}^{3}{}^{t+\Delta t}\ddot{u}_i\delta{}_tu_i + \sum_{i=1}^{2}{}^{t+\Delta t}I_{it}\ddot{\theta}_i\delta{}_t\theta_i + {}^{t+\Delta t}J_t\ddot{\theta}_3\delta{}_t\theta_3\right)\mathrm{d}x_3 - \int_{{}_tL}\sum_{i=1}^{3}{}^{t+\Delta t}f_i\delta{}_tu_i\,\mathrm{d}x_3 = 0 \tag{6} $$

where ${}^{t+\Delta t}\rho$ is the material density and ${}^{t+\Delta t}f_i$ is the distributed force along the beam, respectively.

For application of the aerial refueling hose, the aerodynamic effects of drag and added mass must be included, such that

$$ {}^{t+\Delta t}f = C_D\left({}^{t+\Delta t}\rho_aD/2\right){}^{t+\Delta t}V_\infty^2 + C_m{}^{t+\Delta t}\rho_a{}^{t+\Delta t}A{}^{t+\Delta t}\ddot{u} \tag{7} $$

where ${}^{t+\Delta t}V_\infty$ is the velocity of the freestream of air, ${}^{t+\Delta t}\rho_a$ is the density of the air, D is the hose diameter, C_D is the drag coefficient, C_m is the added mass coefficient, ${}^{t+\Delta t}A$ is the section area of the hose, and ${}^{t+\Delta t}\ddot{u}$ is the acceleration of the hose, respectively. The added mass coefficient will be unity, $C_m=1$, for a circular section hose.

By substituting Eqs. (2–4) and (7) into Eq. (6), we derive the discretized finite element equation of motion of the curved beam element:

$$ \left[{}_t^tM\right]\{{}_t\ddot{u}\} + \left[{}_t^tC\right]\{{}_t\dot{u}\} + \left[{}_t^tK\right]\{{}_tu\} = \{{}^{t+\Delta t}F\} - \left\{{}^tF_S\right\} - \left\{{}^tF_I\right\} - \left\{{}^tF_d\right\} \tag{8} $$

where $[{}_t^tM]$, $[{}_t^tC]$, and $[{}_t^tK]$ are the mass, damping, and stiffness matrixes; $\{{}_t\ddot{u}\}$, $\{{}_t\dot{u}\}$, and $\{{}_tu\}$ are the acceleration, velocity, and displacement vectors; and $\{{}^{t+\Delta t}F\}$, $\{{}^tF_S\}$, $\{{}^tF_I\}$, and $\{{}^tF_d\}$ are the external, initial stress, inertia, and drag load vectors, respectively. The mass matrix includes the added mass of air, and the damping matrix is the combination of air viscous damping and Rayleigh damping (see Ref. 34), such as

$$ \left[{}_t^tM\right] = \left[{}_t^tM_b\right] + \left[{}_t^tM_a\right] $$
$$ \left[{}_t^tC\right] = \left[{}_t^tC_d\right] + \alpha_v\left[{}_t^tM\right] + \beta_v\left[{}_t^tK\right] \tag{9} $$

where $[{}_t^tM_b]$ and $[{}_t^tM_a]$ are the mass matrices of the beam and the added mass of air, $[{}_t^tC_d]$ is the viscous damping of air, and (α_v, β_v) are the Rayleigh damping coefficients, respectively.

The equation of motion (8) will be solved numerically by the predictor–corrector method[31] using a Newmark time-stepping

scheme with a Newton–Raphson iteration. The process of the predictor–corrector method may be outlined as follows:

1) Predict displacement $\{^{t+\Delta t}\boldsymbol{u}^{(i)}\}$, velocity $\{^{t+\Delta t}\dot{\boldsymbol{u}}^{(i)}\}$, and acceleration $\{^{t+\Delta t}\ddot{\boldsymbol{u}}^{(i)}\}$ at time $t+\Delta t$ by

$$\left\{^{t+\Delta t}\boldsymbol{u}^{(i)}\right\} = \{^{t+\Delta t}\tilde{\boldsymbol{u}}\} = \{^{t}\boldsymbol{u}\} + \{^{t}\dot{\boldsymbol{u}}\}\Delta t + \left(\tfrac{1}{2}-\beta\right)\Delta t^2\{^{t}\ddot{\boldsymbol{u}}\} \quad (10)$$

$$\left\{^{t+\Delta t}\dot{\boldsymbol{u}}^{(i)}\right\} = \{^{t+\Delta t}\tilde{\dot{\boldsymbol{u}}}\} = \{^{t}\dot{\boldsymbol{u}}\} + (1-\alpha)\Delta t\{^{t}\ddot{\boldsymbol{u}}\} \quad (11)$$

$$\left\{^{t+\Delta t}\ddot{\boldsymbol{u}}^{(i)}\right\} = \{^{t+\Delta t}\tilde{\ddot{\boldsymbol{u}}}\} = \left(\left\{^{t+\Delta t}\boldsymbol{u}^{(i)}\right\} - \{^{t+\Delta t}\tilde{\boldsymbol{u}}\}\right)\Big/\beta\Delta t^2 = 0 \quad (12)$$

2) Form effective stiffness matrix $[{}_t^t\boldsymbol{K}_e]$ and calculate residual force $\{\boldsymbol{R}({}_t\boldsymbol{u}^{(i)})\}$:

$$\left[{}_t^t\boldsymbol{K}_e\right] = (1/\beta\Delta t^2)\left[{}_t^t\boldsymbol{M}\right] + (\alpha/\beta\Delta t)\left[{}_t^t\boldsymbol{C}\right] + \left[{}_t^t\boldsymbol{K}\right] \quad (13)$$

$$\left\{\boldsymbol{R}\left({}_t\boldsymbol{u}^{(i)}\right)\right\} = \left[{}_t^t\boldsymbol{K}_e\right]\left\{{}_t\boldsymbol{u}^{(i)}\right\} = \{^{t+\Delta t}\boldsymbol{F}\} - \left\{^{t+\Delta t}\boldsymbol{F}_I^{(i)}\right\} - \left\{^{t+\Delta t}\boldsymbol{F}_S^{(i)}\right\} \quad (14)$$

3) Solve for correction $\{{}_t\boldsymbol{u}^{(i)}\}$ and correct previous solutions:

$$\left\{^{t+\Delta t}\boldsymbol{u}^{(i+1)}\right\} = \left\{^{t+\Delta t}\boldsymbol{u}^{(i)}\right\} + \left\{{}_t\mathbf{u}^{(i)}\right\} \quad (15)$$

$$\left\{^{t+\Delta t}\ddot{\boldsymbol{u}}^{(i+1)}\right\} = \left(\left\{^{t+\Delta t}\boldsymbol{u}^{(i+1)}\right\} - \left\{^{t+\Delta t}\tilde{\boldsymbol{u}}\right\}\right)\Big/\beta\Delta t^2 \quad (16)$$

$$\left\{^{t+\Delta t}\dot{\boldsymbol{u}}^{(i)}\right\} = \left\{^{t+\Delta t}\tilde{\dot{\boldsymbol{u}}}\right\} + \Delta t\left\{^{t+\Delta t}\ddot{\boldsymbol{u}}^{(i+1)}\right\} \quad (17)$$

If the residual force or the correction to the displacement is greater than the prescribed tolerance and additional iterations are to be performed, i is replaced by $i+1$, and calculations resume with Eq. (13). In the preceding equations, the α and β are the Newmark's time integration parameters that can be determined by

$$\alpha = (3-\rho_\infty)/2(1+\rho_\infty), \qquad \beta = 1/(1+\rho_\infty)^2 \quad (18)$$

where ρ_∞ is a spectral radius representing the numerical damping in the high-frequency limit (usually user-defined high-frequency dissipation). This numerical dissipation varies from the no dissipation case, $\rho_\infty = 1$, to the so-called asymptotic annihilation case, $\rho_\infty = 0$.

III. Experimental Verification of Element

The newly developed curved beam element and the corresponding finite element codes are validated by the free-swing experiment of an instrumented steel cable. The cable is initially simply supported at both ends by circular pins and then released from the temporary support to allow it swing freely. A high-speed digital camera records the motion of the swinging cable while an oscilloscope records the time history of cable tension at the simply supported end by strain gauges. The selected test piece is a 6.5-mm-diam, 6×7 with 1×7 wire steel core steel cable 1668 mm long. Its effective area and the cross-sectional moment of inertia are 19.62 mm^2 and 2.71 mm^4, respectively. The cable density is 0.15 kg/m, and its elastic modulus is 53 GPa. Two aluminum blocks are attached to each end as harnesses. The dimensions of the free end block are $100\times 50\times 25$ mm, whereas the block at the simply supported end is $45\times 16\times 6$ mm. Four 3.175-mm unidirectional strain gauges were mounted on two opposite faces of the block at the simply supported end in T configurations to eliminate possible out-of-plane bending effects, as well as to increase the gain of the strain gauge readings.

For the motion of a low-tension cable, the drag effect of the free end block becomes noticeable and can be determined as follows:

$$F = -1.1\rho_a D V^2 \quad (19)$$

where D is the characteristic transverse dimension of the block, ρ_a is the air density, and V is the velocity of block, respectively.

The experiment was conducted with an additional lumped mass of 0.34 kg attached to the free end of the cable. The motion of the swinging cable was captured using the high-speed digital camera at every 1/120 s, and the cable tension was measured at the simply supported end by strain gauges at a sampling rate of 1000 Hz. Figure 2 shows the measured position of the free end of the cable vs time. Figure 3 shows the time history of the measurements of cable tension at the simply supported end.

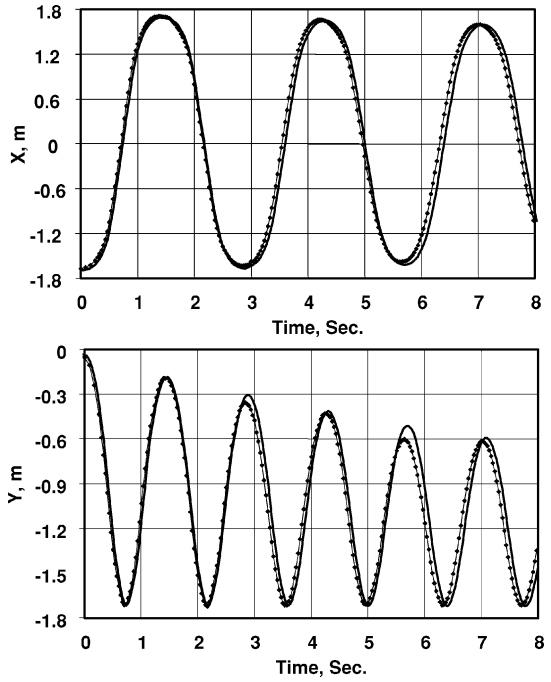

Fig. 2 Test results and finite element predictions of position of free end of swinging cable: ◆, test and ——, new element.

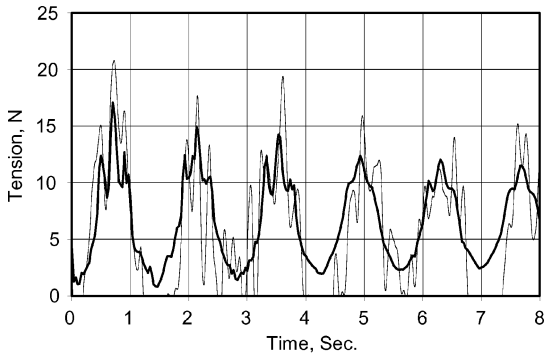

Fig. 3 Comparison of cable tension at simply supported end of swing cable: ——, test and ——, new element.

The finite element analysis of the cable is carried out using 12 newly developed curved beam elements (10 for the cable and 2 for the end blocks) and 1 mass element for the lumped mass. The parameters for time integration, such as the time step, the spectral radius of numerical damping, and Rayleigh damping coefficients, were chosen carefully by examining the dynamic characteristics of the swinging cable. The experimental data of Fig. 2 show that the frequency of pendulum motion of the swing cable is 0.35 Hz and that the logarithmic decrement is 0.02, which is equivalent to a critical damping ratio of 0.003 (Ref. 34). In addition, the membrane natural frequency of the cable is 156 Hz, and its inherent damping is exceptionally low, usually less than 0.002 of critical damping.[35] By the definition of Rayleigh damping (see Ref. 34), we obtain the Rayleigh damping coefficients $\alpha_v \approx 10^{-2}$ and $\beta_v \approx 10^{-5}$. In addition, the work of Kuhl and Crisfield[36] for an elastic pendulum demonstrated that the Newmark integration scheme with $\rho_\infty = 1.0$ is unstable in this class of nonlinear problem. A lower value of the spectral radius, $\rho_\infty < 1.0$, is required to maintain the numerical stability. However, this selection would result in a decrease of total energy of the system. Consequently, a spectral radius of numerical

damping of $\rho_\infty = 0.95$ was selected to provide the minimum required numerical damping to dissipate the spurious high-frequency components while minimizing the loss of the total energy. Finally, the finite element discretization of the cable results in a smallest modal period of 0.0004 s. A stable time step needs to be about 1/10 of the smallest period.[37] Thus, the time integration step was set to 4×10^{-5} s for the finite element analysis.

The predicted time history of position of the free end of cable is shown in Fig. 2 against the experimental findings. Note that the finite element results agree with the experimental data very well. Next, the predicted time history of the cable tension at the simply supported end is shown in Fig. 3 against the experimental results. The finite element predictions and experimental results are again in good agreement.

IV. Simulation of Aerial Refueling Hose and Drogue System

In this section, we demonstrate the ability of the newly developed curved beam in modeling the dynamic characteristics of the system of the aerial refueling hose and drogue. The analysis was done based on the data of a wing–pod refueling hose mounted on a KC-10 refueling tanker. The hose and drogue characteristics are given in Table 1 where $P = \frac{1}{2}\rho_a V_\infty^2$ is the dynamic air pressure and V_∞ is the airstream velocity, respectively.

Because the hose may not perpendicular to the incoming airflow, the aerodynamic drag is decomposed into the normal and tangential components

$$F_n^d = (\rho_a D/2) V_\infty^2 f_n(\theta), \qquad F_t^d = (\rho_a D/2) V_\infty^2 f_t(\theta) \tag{20}$$

where $f_n(\theta)$ and $f_t(\theta)$ are the normal and tangential load functions, respectively. They are functions of the inclination angle θ, Reynolds number, shape of cross section, and surface condition, and they are determined experimentally. The specific aerodynamic loading functions[38] are selected for the study of aerial refueling hose such that

$$f_n(\theta) = 0.02\sin(\theta) + 1.1\sin^2(\theta), \qquad f_t(\theta) = 0.02\cos(\theta) \tag{21}$$

Equation (21) indicates that $C_D = f_n\,(90\text{ deg}) = 1.12$ and $C_{DT} = f_t\,(0\text{ deg}) = 0.02$. For applications with drag coefficients other than 1.12 and 0.02, $f_n(\theta)$ and $f_t(\theta)$ will be factored with an appropriate drag coefficient.

A. Oscillation of Hose and Drogue Due to Disturbance at Towing Point

Consider a tanker flying horizontally with a fully deployed refueling hose 23.77 m (78 ft) long. The hose and drogue system stabilizes to a quasi-static catenary shape. Assume that the tanker experiences a one-half sinusoidal pulse of 0.5 m with $\frac{1}{6}$-s duration in the vertical direction. The dynamic response of the hose and drogue system to the disturbance was analyzed with the newly developed finite element. The hose was modeled by 24 curved beam elements, and the drogue was modeled as a lumped mass. The time integration step was 5×10^{-5} s. The spectral radius for the numerical damping was $\rho_\infty = 0.95$ and the Rayleigh damping coefficients were $\alpha_v = 10^{-3}$ and $\beta_v = 10^{-5}$, respectively, because the axial damping of the hose is very low. Four flying speeds, 103 m/s (200 kn), 116 m/s (225 kn), 131 m/s (255 kn), and 154 m/s (300 kn), were analyzed.

Table 1 Hose and drogue characteristics

Parameter	Value
Air density ρ_a	1.22 kg/m^3
Hose outside diameter D	0.0673 m (2.65 in.)
Hose cross section area A	0.000993147 m^2
Hose density per length m	2.39 kg/m (1.6 lb/ft)
Hose elastic modulus E	336 MPa
Hose drag coefficient C_d	1.2
Drogue mass M	29.5 kg (65 lb)
Drogue drag F_D	$0.232P$ N ($2.5P$ lb)

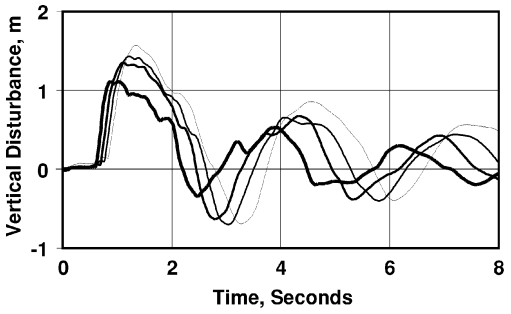

Fig. 4 Vertical displacements of drogue at different flying speeds: ——, 154 m/s; ——, 131 m/s; ——, 116 m/s; and ——, 103 m/s.

The results of finite element analysis are shown in Figs. 4–6. They reveal that the amplitude of a sinusoidal pulse is amplified as it travels downstream. For instance, the vertical displacement at the drogue ranges from 1.1 to 1.6 m/s depending on the flying speed (Fig. 4). Obviously, the pulse is pushed downstream and energized by the airflow; see the wave propagations at 131 m/s (255 kn) in Fig. 5, leading to a hose whipping near the drogue. The travel speed of the pulse along the hose is $c = \sqrt{(T/m)}$, where T and m are the tension and the linear density of the hose, respectively. Because the hose tension is proportional to the drag acting on the drogue, the travel speed of the pulse along the hose is approximately $c \approx 0.243 V_\infty$ for the given hose/drogue system, which is always less than the relative airflow speed V_∞. This indicates that the given hose/drogue system is not stable to the disturbance because any small disturbance caused by the tanker will be amplified along the hose and ultimately lead to hose whipping near the drogue.[8] The hose whipping will generate high-tension spikes in the hose, which is as high as seven times the steady-state tension (Fig. 6) and indicates a high risk of premature separation of the drogue from the hose.

As outlined earlier, it is imperative that the propagation speed of the pulse c be greater than the airflow so that the latter acts as a damping medium to stabilize the hose and drogue system. The most effective way to increase the propagation speed is to increase the drag of the drogue, which in turn increases the hose tension.

Let the pulse propagation speed equal the airflow speed, such that

$$V_\infty = c = \sqrt{T/m}$$

However, the hose tension is approximately equal to the drag of the drogue, such that

$$T \approx F_D = \tfrac{1}{2}\rho_a V_\infty^2 C_d^d$$

where C_d^d is the drag coefficient of the drogue. Then the critical drag coefficient of the drogue for a stable hose and drogue system should be

$$C_d^d = 2m/\rho_a \tag{22}$$

Equation (22) shows that a lighter hose requires less drag at the drogue to stabilize the hose and drogue system.

B. Oscillation of Hose in Coupling Process

Consider the aircraft flying horizontally at 131 m/s (255 kn) with a fully deployed refueling hose of 23.77 m (78 ft) long while a receiver approaches and couples the drogue with its probe by pushing the drogue forward. If the reel-in mechanism fails to take up the slack hose during the drogue and probe coupling process, the hose will slacken, and then violent motion of the hose develops.

To analyze the oscillation of hose in the coupling process, the hose was modeled by 24 curved beam elements with the tow point simply supported and the drogue being pushed forward with a specified time-varying acceleration that represents a typical hookup motion[3] given in Eq. (23) in meters per second squared. The total period of the coupling process lasts 1.25 s:

$$a(t) = \begin{cases} -12.192t, & 0 \le t \le 0.125\text{ s} \\ -1.905 + 3.048t, & 0.125\text{ s} \le t \le 1.125\text{ s} \\ 15.24 - 12.192t, & 1.125\text{ s} \le t \le 1.25 \end{cases} \tag{23}$$

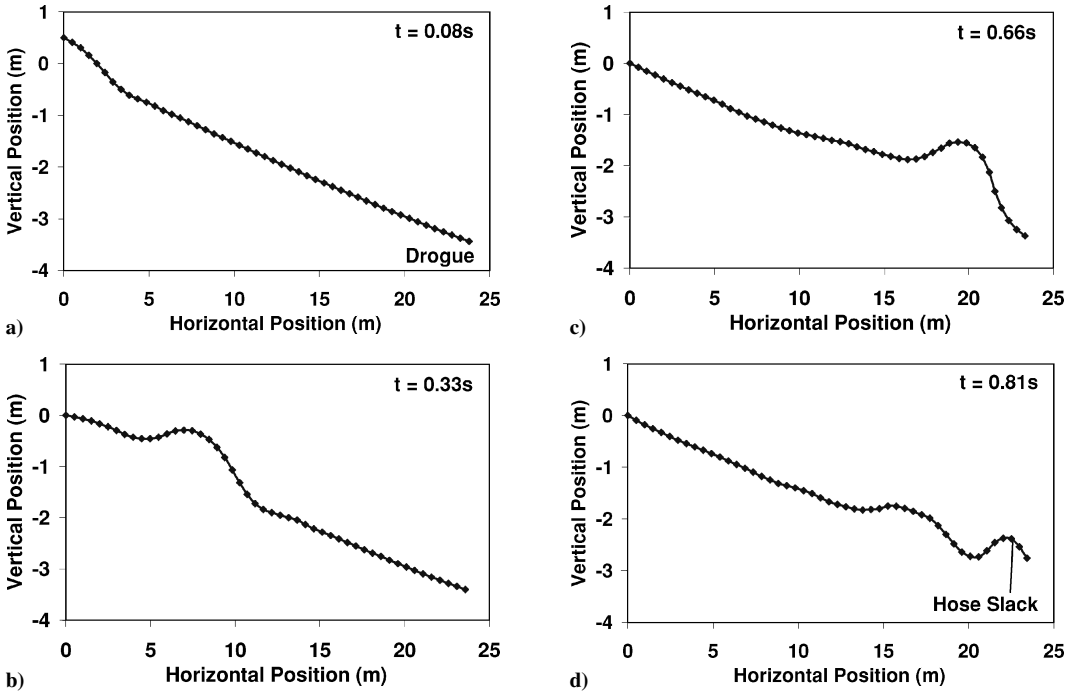

Fig. 5 Wave propagation and whipping of refueling hose near the drogue, $V_\infty = 131$ m/s (255 kn).

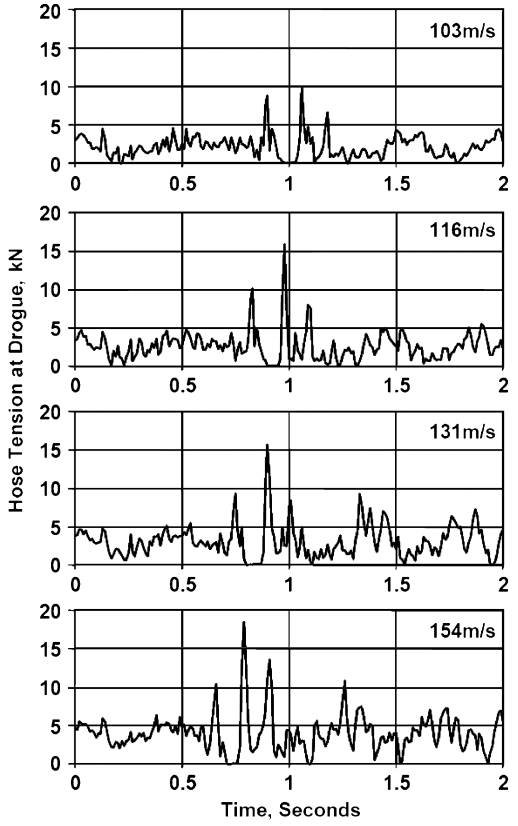

Fig. 6 Hose tension at drogue for different flying speeds.

The time integration step was 5×10^{-5} s. The spectral radius for the numerical damping was $\rho_\infty = 0.95$, and the Rayleigh damping coefficients were $\alpha_v = 10^{-3}$ and $\beta_v = 10^{-5}$, respectively.

The finite element prediction of the hose positions and tension at the drogue are shown in Figs. 7 and 8. It is shown that the hose tension drops to zero rapidly as soon as the probe pushes the drogue forward and the hose slackens. The sag of the hose propagates upwind to the tanker under the interaction of gravity and aerodynamic drag as the probe continues to push the drogue forward and increases the length of the slackening hose. Once the probe stops, a sinusoidal wave is formed and pushed downstream by airflow, resulting in a whipping action of the hose near the drogue. This phenomenon is consistent with field observations.[3] Tension spikes in the hose appear near the drogue as a result of the whipping, which is as high as 4.4 times of the steady-state tension (Fig. 8). It indicates a high risk of premature separation of the drogue from the hose and potential damage to the probe or the receiver aircraft if a malfunction of the reel-in mechanism occurs during the coupling process.

C. Orbiting of Hose and Drogue Due to Vortex-Induced Velocity

The vortex field behind the wing and the storage pod of the hose/drogue system will cause vortices and associated vortex-induced velocity, which may result in three-dimensional oscillations of the hose and the drogue. Because the detailed data of the vortex field behind the wing of KC-10 are not available, a simple, semi-infinite vortex field of the pod is assumed (Fig. 9), and its effect on the hose and the drogue is studied to give qualitative insights into the stability problem of the refueling hose and drogue system.

Assume that the vortex field of the pod is a three-dimensional semi-infinite straight vortex filament trailing behind the pod horizontally. The vortex strength is obtained[3] as $\Gamma_{\text{pod}} = 97.55$ m^2/s (1050 ft^2/s) when the tanker is flying horizontally at 131 m/s (255 kn).

First, a short hose, 1.52 m (5 ft) long, is considered with a drogue, representing a reel failure during the deployment process. The hose is modeled using four new elements, and the drogue is modeled as a lumped mass. The time integration step is 5×10^{-5} s. The spectral radius for the numerical damping is $\rho_\infty = 0.95$, and Rayleigh damping coefficients are $\alpha_v = 10^{-3}$ and $\beta_v = 10^{-5}$. Because of the vortex-induced velocity, the hose and the drogue are subjected to an additional transverse drag around the vortex filament, as shown in Fig. 9. The finite element predictions are shown in Fig. 10. It is shown that the hose and the drogue orbit around the vortex filament like a rigid bar for the short hose after the initial transient period. This motion may result in the drogue hitting the wing trailing edge. The inclination angle between the hose and vortex filament at the steady orbiting state is 37.7 deg with the theoretical calculation. The finite element prediction is 37.1 deg, indicating good accuracy of the finite element results.

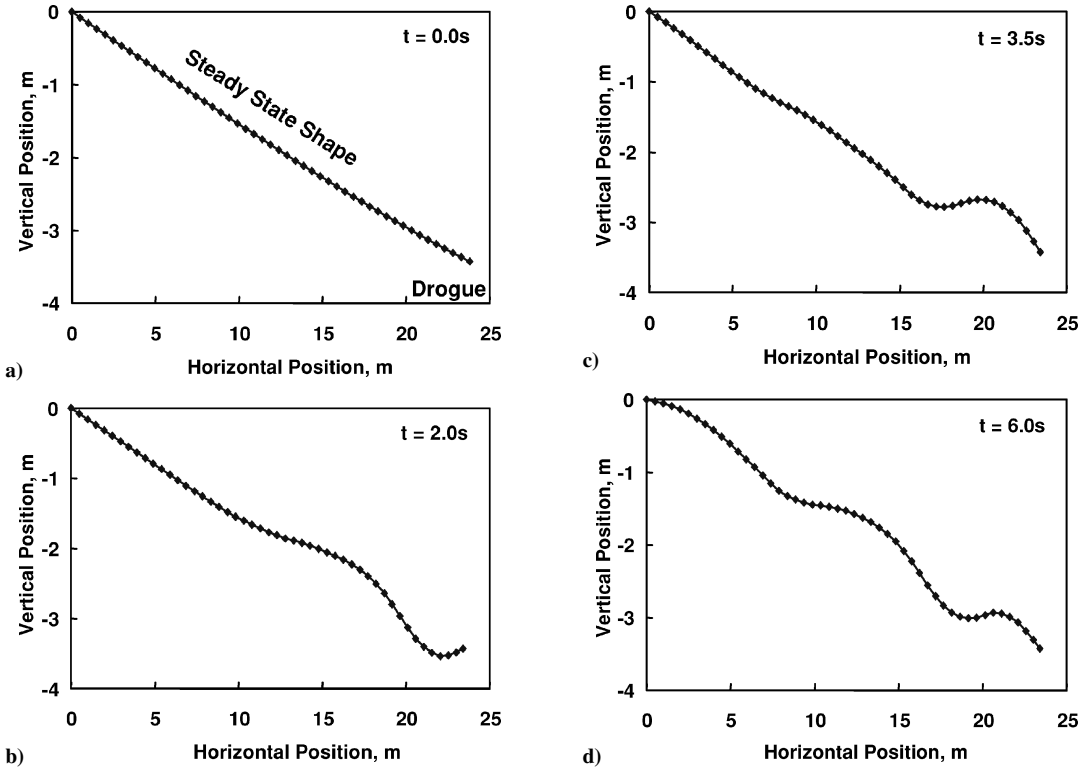

Fig. 7 Wave propagation and whip of refueling hose near drogue during coupling with reel malfunction.

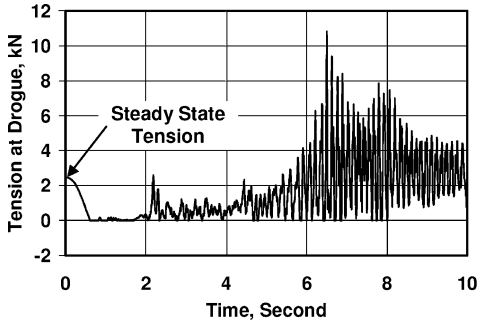

Fig. 8 Predicted hose tension at drogue during coupling with reel malfunction.

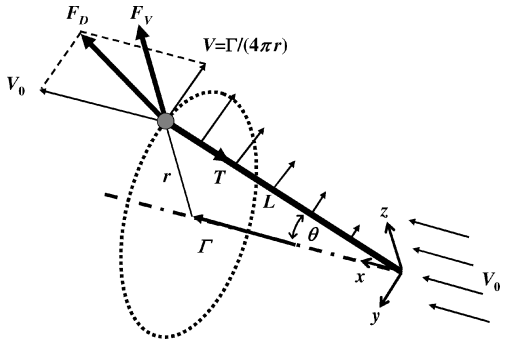

Fig. 9 Interaction of freestream flow and vortex on hose and drogue.

Next, a longer hose of 14.02 m (46 ft) is analyzed. The hose is modeled with 20 curved beam elements. The analysis results are shown in Fig. 11. Unlike the short hose, the long hose orbits in a bow shape with a knot (node) near the drogue and the drogue moves in small circles. This reveals that the vortex has a significant effect on the hose and the drogue. As the length of the hose increases, the vortex has less effect on the drogue. This suggests a fast deployment or recovery of the hose and the drogue to avoid the orbiting motion being fully developed.

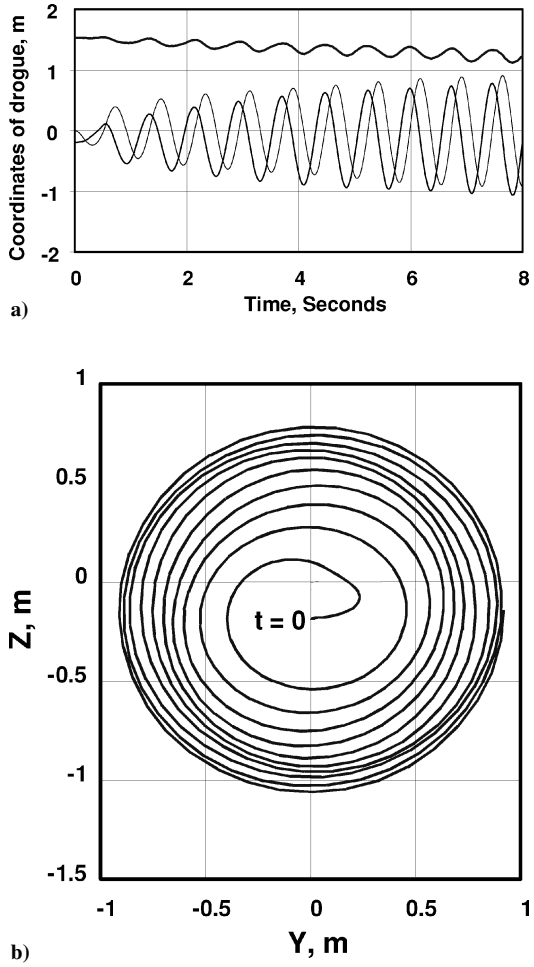

Fig. 10 Simulation results of 1.52-m (5-ft) hose: a) time history of drogue position; ——, X; ——, Y; and ——, Z; and b) rear view of orbiting trajectory of drogue in the vertical plane.

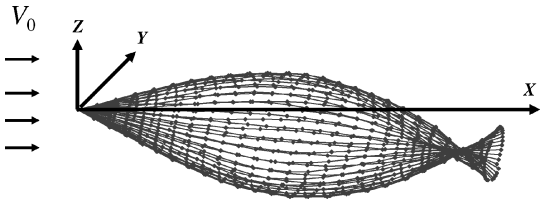

Fig. 11 Simulation results of 14.02-m (46-ft) hose.

V. Conclusions

In this paper, we developed an accurate and computationally efficient three-noded, curved beam element to model an aerial refueling hose. Lower-order consistently coupled polynomial interpolations are used to eliminate the membrane locking and ensure a faster convergence rate. Experiments involving the free swinging of a steel cable were conducted to validate the newly developed curved beam element and the predictor–corrector time integration algorithm. Subsequently, the new element was applied to model and analyze the dynamic behavior of a refueling hose and drogue accounting for 1) the disturbance at the tanker, 2) the hose slackening during the probe/drogue coupling process, and 3) the vortex wake behind the refueling pod. The finite element predictions show the following: 1) A small disturbance at the tanker may be amplified downstream and result in a hose whipping near the drogue if the drag of drogue is not sufficient. 2) A malfunction of the reel-in mechanism during the probe/drogue coupling process will also lead to a hose whipping near the drogue. The whipping results in tension spikes as high as 4.4–7 times the steady-state tension and could lead to premature failure and separation of the drogue from the hose. The study also indicates that the vortex resulting from the pod has a significant impact on the stability of a short refueling hose. This unstable effect decays as the hose length is increased. Compared with the limited data available in the literature, the newly developed curved beam element is shown to be capable of treating the refueling problem accurately and efficiently.

References

[1]Gates, W. R., and McCarthy, M. J., "United States Marine Corps Aerial Refueling Requirements Analysis," *Proceedings of the 2000 Winter Simulation Conference*, edited by J. A. Joines, R. R. Barton, K. Kang, and P. A. Fishwick, Association for Computing Machinery, New York, Inst. of Electrical and Electronics Engineers, Piscataway, NJ, and Society for Computer Simulation International, San Diego, CA, 2000, pp. 1075–1081.

[2]Smith, R. K., *Seventy-Five Years of Inflight Refueling, Highlights 1923 to 1998*, U.S. Air Force History and Museums Program, Washington, DC, 1998.

[3]Vassberg, J. C., Yeh, D. T., Blair, A. J., and Evert, J. M., "Dynamic Characteristics of a KC-10 Wing-Pod Refueling Hose by Numerical Simulation," AIAA Paper 2002-2712, June 2002.

[4]Vachon, M. J., and Ray, R. J., "Calculated Drag of an Aerial Refueling Assembly Through Airplane Performance Analysis," NASA TM-2004-212043, Feb. 2004.

[5]Bairstow, L., Relf, E. F., and Jones, R., "The Stability of Kite Balloons: Mathematical Investigation," Aeronautical Research Council, RM 208, London, Dec. 1915.

[6]Glauert, H., "The Stability of a Body Towed by a Light Wire," Aeronautical Research Council, RM 1312, London, Feb. 1930.

[7]DeLaurier, J. D., "A Stability Analysis for Tethered Aerodynamically Shaped Balloons," *Journal of Aircraft*, Vol. 9, No. 9, 1972, pp. 646–651.

[8]Phillips, W. H., "Theoretical Analysis of Oscillations of a Towed Cable," NACA TN 1796, Jan. 1949.

[9]DeMatteis, G., "Dynamics of a Towed Sailplane," AIAA Paper 91-2862, 1991.

[10]Nakagawa, N., and Obata, A., "Longitudinal Stability Analysis of Aerial Towed Systems," *Journal of Aircraft*, Vol. 29, No. 6, 1992, pp. 978–985.

[11]Burgess, J. J., "Equations of Motion of a Submerged Cable with Bending Stiffness," *Offshore Marine and Arctic Engineering*, Vol. 1-A, Jan. 1992, pp. 283–289.

[12]Howell, C. T., "Numerical Analysis of 2-D Nonlinear Cable Equations with Applications to Low-Tension Problems," *International Journal of Offshore and Polar Engineering*, Vol. 2, No. 2, 1992, pp. 110–113.

[13]Buckham, B., and Nahon, M., "Dynamics Simulation of Low Tension Tethers," *Proceedings of the OCEANS'99 MTS/IEEE*, Oceans'99 MTS/IEEE Conf. Committee, Washington, DC, 1999, pp. 757–766.

[14]Koh, C. G., Zhang, Y., and Quek, S. T., "Low-Tension Cable Dynamics: Numerical and Experimental Studies," *Journal of Engineering Mechanics*, Vol. 125, No. 3, 1999, pp. 347–354.

[15]Wu, Q., Takahashi, K., and Nakamura, S., "Non-Linear Vibrations of Cables Considering Loosening," *Journal of Sound and Vibration*, Vol. 261, No. 3, 2003, pp. 385–402.

[16]Zhu, Z. H., Meguid, S. A., and Ong, L. S., "Dynamic Multiscale Simulation of Towed Cable and Body," *Proceedings of the Second MIT Conference on Computational Fluid and Solid Mechanics*, edited by K. J. Bathe, Elsevier, 2003.

[17]Schrefler, B. A., and Odorizzi, S., "A Total Lagrangian Geometrically Nonlinear Analysis of Combined Beam and Cable Structures," *Computer and Structures*, Vol. 17, No. 1, 1983, pp. 115–127.

[18]Reddy, J. N., "On Locking-Free Shear Deformable Beam Finite Elements," *Computer Methods in Applied Mechanics and Engineering*, Vol. 149, No. 1–4, 1997, pp. 113–132.

[19]Chakraborty, A., Gopalakrishnan, S., and Reddy, J. N., "A New Beam Finite Element for the Analysis of Functionally Graded Materials," *International Journal of Mechanical Sciences*, Vol. 45, No. 3, 2003, pp. 519–539.

[20]Cantin, G., and Clough, R., "A Curved Cylindrical Shell Finite Element," *AIAA Journal*, Vol. 6, No. 6, 1968, pp. 1057–1062.

[21]Laulusa, A., and Reddy, J. N., "On Shear and Extensional Locking in Nonlinear Composite Beams," *Engineering Structures*, Vol. 26, No. 2, 2004, pp. 151–170.

[22]Stolarski, H., and Belytschko, T., "Membrane Locking and Reduced Integration for Curved Elements," *Journal of Applied Mechanics*, Vol. 49, No. 1, 1981, pp. 172–178.

[23]Prathap, G., and Bhashyam, G. R., "Reduced Integration and the Shear Flexible Beam Element," *International Journal for Numerical Methods in Engineering*, Vol. 18, No. 2, 1982, pp. 195–210.

[24]Prathap, G., and Bhashyam, G. R., "A Linear Thick Curved Beam Element," *International Journal for Numerical Methods in Engineering*, Vol. 23, No. 7, 1986, pp. 1313–1328.

[25]Balasubramanian, T. S., and Prathap, G., "A Field Consistent Higher-Order Curved Beam Element for Static and Dynamic Analysis of Stepped Arches," *Computers and Structures*, Vol. 33, No. 1, 1989, pp. 281–288.

[26]Raveendranath, P., Singh, G., and Pradhan, B., "A Two-Noded Locking-Free Shear Flexible Curved Beam Element," *International Journal for Numerical Methods in Engineering*, Vol. 44, No. 3, 1999, pp. 265–280.

[27]Bucalem, M. L., and Bathe, K. J., "Locking Behavior of Isoparametric Curved Beam Finite Elements," *Applied Mechanics Review*, Vol. 48, No. 2, 1995, pp. S25–S29.

[28]Raveendranath, P., Singh, G., and Pradhan, B., "Free Vibration of Arches Using a Curved Beam Element Based on a Coupled Polynomial Displacement Field," *Computers and Structures*, Vol. 78, No. 4, 2000, pp. 583–590.

[29]Raveendranath, P., Singh, G., and Rao, G. V., "A Three-Noded Shear-Flexible Curved Beam Element Based on Coupled Displacement Field Interpolations," *International Journal for Numerical Methods in Engineering*, Vol. 51, No. 1, 2001, pp. 85–101.

[30]Zhu, Z. H., and Meguid, S. A., "Analysis of Three-Dimensional Locking-Free Curved Beam Element," *International Journal of Computational Engineering Science*, Vol. 5, No. 3, 2004, pp. 535–556.

[31]Hughes, T. J. R., Pister, K. S., and Taylor, R. L., "Implicit–Explicit Finite Elements in Nonlinear Transient Analysis," *Computer Methods in Applied Mechanics and Engineering*, Vol. 17/18, No. 1, 1979, pp. 159–182.

[32]Choi, J., and Lim, J., "General Curved Beam Elements Based on the Assumed Strain Fields," *Computers and Structures*, Vol. 55, No. 3, 1995, pp. 379–386.

[33]Zhu, Z. H., "Nonlinear Elastodynamic Analysis of Low Tension Cable Using a New Beam Element," Ph.D. Dissertation, Mechanical and Industrial Dept., Univ. of Toronto, Toronto, Sept. 2004.

[34]Rao, S. S., *Mechanical Vibrations*, 3rd ed., Addison Wesley Longman, New York, 1995.

[35]Carrie, T. G., "Guy Cable Design and Damping for Vertical Axis Wind Turbines," Sandia National Labs., National Technical Information Service Rept. SAND80-2669, U.S. Dept. of Commerce, May 1980.

[36]Kuhl, D., and Crisfield, M. A., "Energy-Conserving and Decaying Algorithms in Non-Linear Structural Dynamics," *International Journal for Numerical Methods in Engineering*, Vol. 45, No. 5, 1999, pp. 569–599.

[37]Bathe, K. J., *Finite Element Procedures in Engineering Analysis*, Prentice–Hall, Englewood Cliffs, NJ, 1982.

[38]Etkin, B., "Stability of a Towed Body," *Journal of Aircraft*, Vol. 35, No. 2, 1998, pp. 197–205.

K. Shivakumar
Associate Editor